Journal of Materials Chemistry B

ROYAL SOCIETY OF CHEMISTRY

PAPER

View Article Online
View Journal | View Issue

Cite this: J. Mater. Chem. B, 2023, 11, 5142

Rod-to-sphere elemental reconstruction of biocompatible Ag_2Te–$Ag_{4.53}$–Te_3 nanoparticles for triple negative breast cancer photo-nanotherapy†

Hojung Ahn,‡[a] Seounghun Kang,‡[b] Kyungtae Kang,[c] Do Nam Lee, *[d] Dal-Hee Min *[be] and Hongje Jang *[a]

Received 12th February 2023,
Accepted 12th May 2023

DOI: 10.1039/d3tb00297g

rsc.li/materials-b

Silver nanoparticles (AgNPs) continue to be applied to agricultural and medical applications because of their antibacterial and antifungal effects. However, AgNPs are vulnerable to poisoning by oxidation or sulfidation, and unintentional toxicity can occur *via* leaching. Therefore, ensuring the stability of AgNPs for practical applications is considered an important requirement. In this study, we propose the solvothermal galvanic replacement of a Te nanorod (TeNR) template with a Ag precursor to manufacture highly stable and biocompatible Ag–Te nanoparticles (AgTeNPs). In addition to their high stability, AgTeNPs composed of Ag_2Te–$Ag_{4.53}Te_3$ were evaluated as a nanotherapeutic agent enabled by their selective toxicity through metabolic degradation in breast cancer cells. It has been demonstrated that combinatorial treatment with hyperthermic cancer-cell ablation through photothermal conversion provides an effective cancer treatment *in vitro* and *in vivo*. The discovered new biocompatible Ag nanomaterials with innate anticancer effects are expected to be applied to various application fields.

Introduction

AgNPs are noble metal nanoparticles with tunable size and shape through various synthesis strategies, and have found a wide range of applications due to their excellent antibacterial effects and surface-enhanced Raman spectroscopic enhancement.[1–3] However, it is difficult to store or use them for a long time under ambient conditions due to their vulnerability to oxidation,[4,5] and there are also critical problems that is they cause cytotoxicity to normal cells by oxidative stress, DNA damage and cytokine induction.[6,7] In addition, AgNPs have a lower reduction potential compared to other precious metal elements such as Au, Pt, and Pd, making them an attractive template for the fabrication of complex nanostructures such as hollow nanoshells, nanocages, and porous nanoparticles.[8,9] The nanoparticles composed of noble metals and Ag alloy through galvanic replacement exhibit negligible toxicity compared to pristine Ag, making them highly suitable for biomedical applications.[10–12] Efforts to achieve safe and efficient Ag nanomaterials by regulating Ag dissolution under physiological condition are continuously made through the design of various compositions or surface coatings with biocompatible layers.

Breast cancer is one of the most common forms of cancer mainly occurring in the lactiferous duct and lobules of breast tissue.[13,14] Because many breast cancer patients are present worldwide, numerous treatment strategies including laparoscopic surgery, radiotherapy, and targeted drug delivery have been developed in recent decades to overcome it.[15,16] Unfortunately, breast cancer has a high expression level of proteins that affects the growth and development of tumor such as epidermal growth factor (EGF) and vascular endothelial growth factor (VEGF), and contribute to rapid proliferation and frequent metastasis with recurrence.[17,18] AgNPs have also been receiving attention as a potential candidate for breast cancer nanotherapeutics due to the feature of EGF and VEGF down-regulation and tumor microenvironment control.[19,20] However, the preclinical and clinical trials of AgNPs were limited because AgNPs, which are susceptible to external physical and chemical stimuli, showed rapid deterioration in stability in a physiological environment and may cause severe toxicity to normal tissues.[21,22]

[a] Department of Chemistry, Kwangwoon University, 20 Gwangwoon-ro, Nowon-gu, Seoul 01897, Republic of Korea
[b] Department of Chemistry, Seoul National University, Seoul 08826, Republic of Korea
[c] Department of Applied Chemistry, Kyung Hee University, 1732 Deogyeong-daero, Yongin, Gyeonggi 17104, Republic of Korea
[d] Ingenium College of Liberal Art (Chemistry), Kwangwoon University, 20 Gwangwoon-ro, Nowon-gu, Seoul 01897, Republic of Korea
[e] Institute of Biotherapeutics Convergence Technology, Lemonex Inc., Seoul 08826, Republic of Korea

† Electronic supplementary information (ESI) available. See DOI: https://doi.org/10.1039/d3tb00297g

‡ These authors contributed equally.

In this study, we synthesized biocompatible Ag–Te nanoparticles (AgTeNPs) and evaluated the nano- and photo-therapeutic efficacy against breast cancer. Instead of using Ag as a sacrificial template for the galvanic replacement reaction as in the conventional way, we successfully synthesized elliptical nanoparticles by applying Ag as the replacing element. A solvothermal environment in ethylene glycol (EG), a polar protic solvent with a reducing moiety, was introduced to perform galvanic replacement using Te nanorods (TeNRs) as a template. During the reaction, unlike previous reports, disintegration was observed through spontaneous atomic diffusion and Ostwald ripening after the formation of the Ag_2Te intermediate rather than conventional elemental replacement. The prepared nanoparticles had elliptical shape with uniformly distributed Ag and Te, and consisted of the $Ag_{4.53}Te_3$ core domain and the Ag_2Te surface crystal region. Due to the Ag_xTe_y compositions, excellent colloidal stability without Ag dissolution was verified, and there was highly efficient photothermal conversion from overall absorption in the ultraviolet (UV), visible (Vis), and near-infrared (NIR) regions. As a result of *in vitro* tests, AgTeNPs showed selective cytotoxicity against highly metabolized breast cancer cells. In addition, photothermal conversion by 808 nm NIR laser irradiation induced hyperthermic ablation in the designated region. AgTeNPs also demonstrated significant cancer therapeutic effects in mouse models.

Results and discussion

The synthesis of AgTeNPs was achieved through solvothermal galvanic replacement using TeNR as a sacrificial nanotemplate (Fig. 1). It has been known that a spontaneous galvanic replacement at room temperature can be accomplished on account of the standard reduction potential difference between Te ($Te^{4+}|Te^0$ = 0.57 V *vs.* standard hydrogen electrode (SHE)) and Ag ($Ag^+|Ag^0$ = 0.7991 V *vs.* SHE), and subsequent manufacturing of Ag_2Te nanorods through synthesis methods was reported previously.[23] TeNR templates are synthesized through the reaction between the tellurite (TeO_3^{2-}) precursor and hydrazine in EG as the solvent, and a purification step is generally required for reproducibility in subsequent reactions, such as galvanic replacement.[21] However, the colloidal stability of Te^0 nanomaterials, which are susceptible to oxidation in air, is rapidly reduced after purification, and thus reproducible morphology and yields cannot be guaranteed. Herein, we applied a well-established approach that involves galvanic replacement in the presence of mild reducing additives (*e.g.* citrate or ascorbic acid) or solvents (*e.g.* EG) having multiple hydroxyl functional groups contributing to the formation of distinctive anisotropic nanostructures and to the prevention of structural collapse under harsh conditions.

By performing the optimized reaction for 2 h at 200 °C in the EG solvent with the Ag/Te atomic ratio of 1.00, AgTeNPs were successfully synthesized. According to the UV-Vis spectroscopic measurement, distinctive two peaks of TeNR nanotemplates around 278 nm (Te p-bonding valence band to p-antibonding conduction band transition) and 608 nm (Te p-lone pair valence band to p-antibonding conduction band transition) disappeared due to the loss of their crystalline trigonal Te (t-Te) feature (Fig. 2a; dotted line).[24–26] AgTeNPs showed an overall downward spectrum with no particular strong absorption peak except for a slight shoulder around 308 nm (Fig. 2a; solid line). AgTeNPs synthesized through solvothermal galvanic replacement showed excellent absorption, whereas most of the previously reported silver telluride quantum dots or nanocrystals exhibited a rapid decrease in the NIR region after 700 nm wavelength.[27,28]

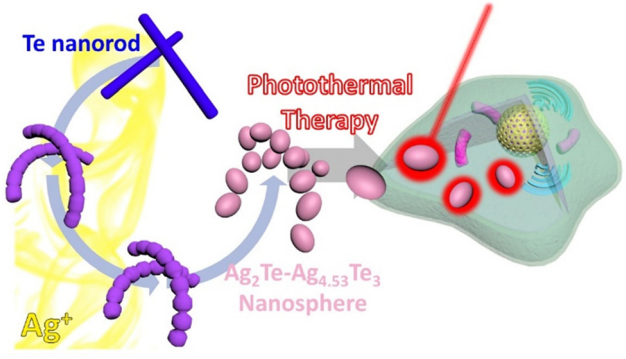

Fig. 1 Schematic illustration of the synthesis AgTeNPs and photo-nano breast cancer therapy.

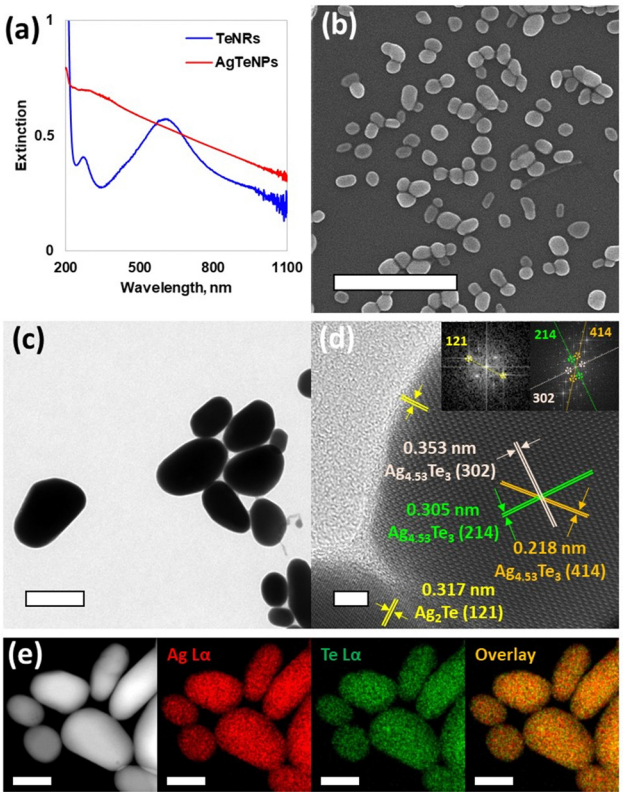

Fig. 2 Characterization of AgTeNPs. (a) UV-Vis spectrum of AgTeNPs. (b) SEM image of the synthesized AgTeNPs. The scale bar is 500 nm. (c) Normal TEM and (d) HR-TEM images of AgTeNPs. (inset: FFT image for Ag_2Te (left) and $Ag_{4.53}Te_3$ section (right)) The scale bars are 100 nm and 5 nm for c and d, respectively. (e) HAADF-STEM/EDS mapping images. The scale bar is 100 nm.

Notable structural changes were confirmed through electron microscopic observations. The general galvanic replacements form a hollow interior structure or porous-protruding surface morphology to the extent that the sacrificial nanotemplate structure is maintained. However, what was confirmed in the low magnification scanning electron microscope image (SEM) was the formation of elliptical nanoparticles (Fig. 2b). A solid internal structure was confirmed through normal transmission electron microscopy (TEM) images, and the major and minor axis length distributions of elliptical nanoparticles (counting NPs number was 50) were calculated as 84.4 ± 7.3 nm and 47.8 ± 3.5 nm, respectively (Fig. 2c).

Next, a more detailed characterization of crystallinity and composition was performed prior to the introduction of the AgTeNPs formation mechanism. In galvanic replacement, when nanotemplates composed of materials such as Ag, Cu, or even Te are used, it is common to observe highly polycrystalline structures rather than single nanocrystalline characteristics due to simultaneous replacement reactions occurring on the surface of the nanotemplates. Interestingly, from the high-resolution (HR) TEM image, AgTeNPs exhibit only two types of highly crystalline phases that are not polycrystalline. The core domain of AgTeNPs exhibited *d*-spacings of 0.353 nm, 0.305 nm, and 0.218 nm which corresponded to the lattice planes (302), (214), and (414) of $Ag_{4.53}Te_3$ (hexagonal; $P\bar{6}2m$), respectively. In contrast, the outer surface of AgTeNPs was identified as Ag_2Te with a monoclinic structure ($P2/c$). this identification was based on the observation of a d-spacing of 0.317 nm corresponding to the lattice plane (121) (Fig. 2d). Using the chemical formula, the Ag/Te atomic ratio of each crystal was 1.51 ($Ag_{4.53}Te_3$) and 2 (Ag_2Te) for the outer surface and core domain, respectively. A relatively large amount of Ag existed on the outer surface compared to the core, which might imply that Ag is introduced into the TeNRs template as outer diffusion and replacement reactions proceeded.

From high angle annular dark field (HAADF) STEM and energy dispersive spectroscopy (EDS) mapping, it was confirmed that Ag and Te were distributed very evenly over the entire AgTeNPs area (Fig. 2e). In galvanic replacement, an alloy composition between the template element and the introduced element is generally formed, but the distribution tends to become discontinuous due to structural disproportionation caused by the stoichiometric balance between the two elements. Therefore, it was inferred from the observations that the solvothermal reaction conditions with sufficient temperature induced topotactic transition, which would result in overall changes in elemental distribution, crystallinity, and particle size and morphology.

Prior to the supposing plausible mechanism, we further verified the crystalline structure and compositional information using X-ray analysis techniques. X-ray photoelectron spectroscopy (XPS) analysis revealed sharp Ag 3d peaks at 367.7 eV and 373.7 eV for $3d_{5/2}$ and $3d_{3/2}$ with a well separated spin–orbit component (Δ_{Ag} = 6.0 eV) (Fig. 3a and Fig. S1, ESI†). The significant peaks at 572.1 eV (Te $3d_{5/2}$) and 582.5 eV (Te $3d_{3/2}$) indicated the Ag–Te bond. In contrast, weak peaks at 575.6 eV (Te^{4+} $3d_{5/2}$) and 586.1 eV (Te^{4+} $3d_{3/2}$) revealed partially oxidized

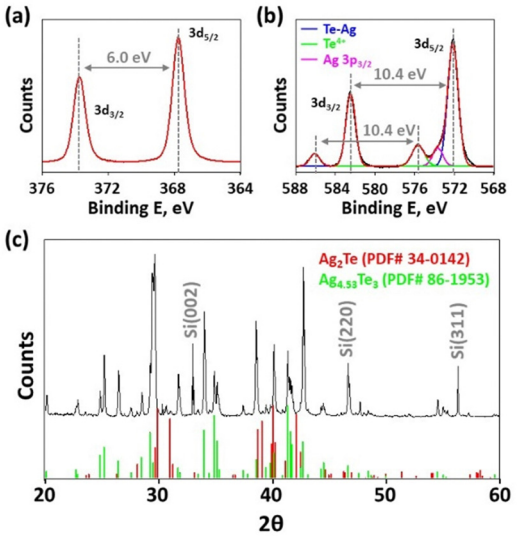

Fig. 3 X-ray characterization of AgTeNPs. Narrow scan XPS spectra of (a) Ag 3d and (b) Te 3d. Intervals indicated by the gray arrows represent the separated spin–orbit components for Ag and Te. (c) XRD pattern of AgTeNPs clearly shows the co-existence of Ag_2Te and $Ag_{4.53}Te_3$ from their reference peaks.

Te components on the outermost surface (Fig. 3b).[29,30] The Te XPS peaks also exhibited a clear spin–orbit component (Δ_{Te} = 10.4 eV), and the asymmetry in the Te $3d_{5/2}$ region originated from superposition with the Ag $3p_{3/2}$ peak (573.7 eV; magenta). The surface of AgTeNPs was covered with poly(vinylpyrrolidone) (PVP), and this was confirmed by deconvoluted C 1s and O 1s XPS spectra (Fig. S2, ESI†).[31]

The X-ray diffraction (XRD) pattern provided more direct and clear evidence for the composition and crystallinity of AgTeNPs. We applied AgTeNPs synthesized under optimized conditions on piranha treated silicon wafer and performed film XRD analysis. The highly crystalline AgTeNPs showed a distinctive XRD pattern, and all identified peaks could be assigned to Ag_2Te (PDF# 34-0142) and $Ag_{4.53}Te_3$ (PDF# 86-1953) (Fig. 3c). The sharp peaks at 2θ = 33.0°, 46.5°, and 56.3° are assigned to the (002), (220), and (311) lattices of Si from the AgTeNPs film supporting material.[32]

In order to reveal the significant structural change from nanorods to nanoellipses accompanying the replacement reaction and to confirm the optimized synthetic conditions, the amount of the Ag cation was set as a variable. When a smaller amount of Ag (Ag/Te = 0.50) was added under the conditions in which AgTeNPs were formed, straight nanorods undergoing oxidative decomposition were observed with sparse irregular nanospheres.[33] When Ag with a higher concentration was added (Ag/Te = 2.00), curved nanorods and partial surface growth were observed instead of monodisperse ellipse AgTeNPs. Afterwards, it was observed that small spherical substructures increased on the surface of the as-formed rod-like morphology as Ag concentration increased (Ag/Te = 4.00). Considering the reducing EG solvent and high temperature environment, it is understood that it was based on the sequential reductive growth of residual Ag cations during

galvanic replacement (Fig. S3, ESI†). We investigated the synthetic mechanism by comparing the product in which 4 times higher amount of Ag cation was added to the reaction (denoted as AgTeNPs-4; Ag/Te = 4.00 in Fig. S3, ESI†) based on the elliptical AgTeNPs (AgTeNPs-1).

According to the inductively coupled plasma mass spectrometry (ICP-MS) analysis, as the amount of Ag added for solvothermal galvanic replacement increases, the actual Ag content constituting AgTeNPs also increases (Fig. S4, ESI†). The observations revealed that the formation of elliptical nanoparticles was only achieved below a certain Ag cation concentration, and a sharp increase in the Ag content was observed under the maximum test concentration, suggesting that the phase shift exists. Considering that only the proportion of Ag was increased under the fixed amount of Te, it is understood that the excess residual Ag in the solution was reduced by EG to grow Ag nanoparticles on the surface. In addition, due to a large amount of Ag, Ag_2Te with a high Ag/Te bonding ratio could be the main component in AgTeNPs-4. According to the XRD analysis result, it was confirmed that AgTeNPs-4 consists only of Ag_2Te and metallic Ag nanoparticles without $Ag_{4.53}Te_3$ (Fig. S5a, ESI†). HAADF-STEM/EDS mapping and HR-TEM images additionally supported the compositional aspect of AgTeNPs-4. Most of the observed particles consisted of Ag, and elliptical nanoparticles composed of Ag_2Te were partially identified (Fig. S5b and c, ESI†).

It was interpreted that solvothermal treatment induces a secondary structural change in addition to accelerating the galvanic replacement reaction rate due to the difference in the structure of the formed nanoparticles specifically in terms of maintaining the rod-shape or forming disconnected nanoellipses. A seed-growth mechanism consisting of nanoseed formation by the reduction of precursor cations using a reducing agent and a subsequent growth process below the threshold precursor concentration has been accepted in most of the nanoparticle synthesis strategies.[34] However, in the process of interpreting the violet-black color nuclei observed in the LaMer and Dinegar mechanism represented by conventional gold nanoparticles, the newly proposed disintegration of the nanowire intermediate provides a new perspective.[35] Moreover, the synthetic mechanism of present AgTeNPs was also confirmed to involve nanowire intermediate disintegration. To verify the hypothesis, we investigated the particle morphology and UV-Vis spectra according to the reaction time under the conditions of Ag/Te = 1.00 and 200 °C applied to the optimized synthesis of AgTeNPs (Fig. S6, ESI†). As the reaction proceeded, the straight TeNRs changed to Ag_2Te nanorods, and secondary surface growth and curvature were achieved. From 30 min of reaction, irregular and convex nanoworms were generated, confirming that reconstruction works. After 30 min, full-scale disintegration occurred, and the concave and narrow domains were completely cut off to form independent elliptical AgTeNPs (Fig. S6, ESI†).

A series of changes can be interpreted using the phase diagram of Ag-Te (Fig. 4a and b).[36,37] According to the diagram, β-Ag_2Te, β-$Ag_{1.9}Te$, and α-Ag_5Te_3 can be formed based on the Ag/Te ratio at the optimized reaction temperature of 200 °C. Most of the tellurite ions in the solution were consumed during

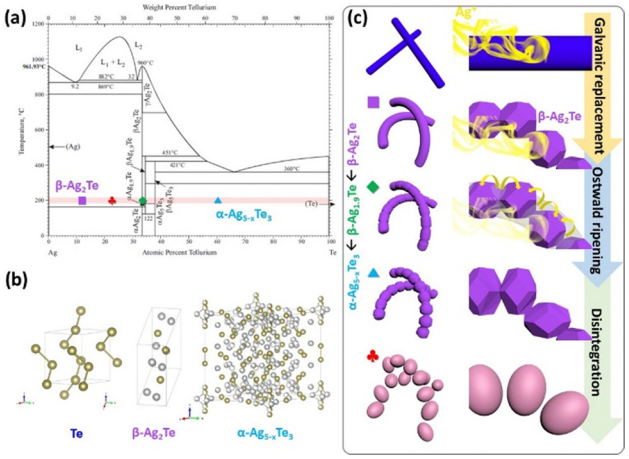

Fig. 4 Plausible mechanism for AgTeNPs formation. (a) Phase diagram for Ag–Te was reprinted with permission from ref 34. For clarity, the reaction temperature is marked with the red band, and several characteristic points are marked with symbols. Copyright 2009 Elsevier. (b) Crystal structure of Te, β-Ag_2Te, and α-$Ag_{5-x}Te_3$.[35] (c) Sequential processing of galvanic replacement of TeNRs with Ag(I), curvature nanoworm formation, Ostwald ripening, and disintegration induced the formation of elliptical AgTeNPs.

the formation of TeNRs, and the atomic percent of Te belongs to a very low area when the Ag cation is added. In this process, reductive Ag deposition and Ag_2Te formation by galvanic replacement occurred, and the Te percent in the solution rose due to the dissolution of Te and consumption of Ag. β-Ag_2Te (monoclinic) and Ag (cubic) introduced into the TeNRs (hexagonal) induced geometrically restricted coalescence of two adjacent crystal facets, forming a non-linear nanoworm (Fig. 4c, ■). Afterwards, the remaining Ag cations in the solution were deposited in the concave cavity of the nanoworm, forming nanocrystals connected by non-crystalline packing (repeatedly convex nanoworm morphology generation, 30 min of reaction) (Fig. 4c, ♦). Following Ostwald ripening, the non-crystalline domains were crystallized into $Ag_{5-x}Te_3$ to form a core domain of AgTeNPs (Fig. 4c, ▲). The contact area was narrowed and separated into stable elliptical AgTeNPs. Through the reconstruction, a significant portion of the Te component was consumed to generate $Ag_{5-x}Te_3$ nanocores, and the phase equilibrium shifted during the process of Ag_2Te surface shell formation (Fig. 4c, ♣). As in the case of Au, surface atomic diffusion and Rayleigh instability enabled the disintegration of hexagonal $Ag_{4.53}Te_3$ nanoworms into AgTeNPs under solvothermal conditions.[38,39]

In general, a proportional relationship between the reaction rate and the temperature is accepted, and to confirm that intermediate disintegration is feasible at a sufficiently high temperature, we performed temperature controlled AgTeNPs synthesis (Ag/Te = 1.00). At room temperature, as in previously reported cases, Ag_2Te nanorods were uniformly evolved, and bending due to coalescence was also observed (Fig. S7, Room Temp., ESI†). It was confirmed that nanocrystals were formed at regular intervals on the surface of Ag_2Te nanorods-like bean pods at 50 °C. As the reaction temperature increases, the depletion of the junctions was caused by Ostwald ripening,

and it proceeded with the formation of spherical or elliptical independent nanostructures (Fig. S7, ESI†).

Prior to *in vitro* and *in vivo* cancer therapeutic evaluation, the colloidal stability and biocompatibility of AgTeNPs were confirmed. In both 1x phosphate buffered saline (PBS) and complete cell culture media, including DI water applied for long-term storage, AgTeNPs showed perfect colloidal stability for 24 h (Fig. S8 and S9, ESI†). Biocompatibility was identified through cytotoxicity evaluation on three different cell lines, non-tumorigenic epithelial cell MCF-10A, triple-negative breast cancer cell MDA-MB-231, and estrogen receptor positive breast cancer cell MCF-7 to confirm both normal and cancer cells. According to the viability assay, MCF-7, which represented the most active cell metabolism and proliferation among the target cell lines, resulted in lowest viability (69.4%) under the condition of 12.5 mg Ag per L of AgTeNPs treatment (Fig. S10, ESI†). MDA-MB-231 showed a slightly higher cell viability (80.5%) under the same conditions, and MCF-10A, a normal cell with the slowest proliferation, was almost unaffected (96.4%).[40–43]

For a detailed interpretation of the identified cytotoxicity differences against cell lines, cell apoptosis assays and apoptotic protein analysis were performed (Fig. S11, ESI†). As the dose of the AgTeNPs treated on MCF-7 increased, the proportion of apoptotic and dead cells increased dramatically, and similar tendency was observed for MDA-MB-231, although to a lesser extent. In contrast, MCF-10A exhibited only 7.2% of apoptotic cells and 7.6% of dead cells even in the maximum dose condition (Fig. 5a–c). According to the apoptosis protein marker analysis against pro-caspase-3, cleaved-caspase-3, and B-cell lymphoma-2 (Bcl-2) against household protein glutamate dehydrogenase (GDH), the dose-dependent downregulation of cell apoptosis inhibitors (pro-caspase-3 and Bcl-2) and upregulation of apoptosis indicator (cleaved-caspase-3) were clearly observed (Fig. 5d and Fig. S12a–c, ESI†).[44,45] The same trend was observed in MDA-MB-231, while a markedly weak band was revealed for MDF-10A, a normal cell line (Fig. 5e, f and Fig. S12d–I, ESI†). It was inferred that the difference in cytotoxicity according to cell types is directly related to the activity of cell metabolism known in the order of MCF-7, MDA-MB-231, and MCF-10A. The verification was made through the quantitative analysis of the amount of AgTeNPs introduced into the cell by ICP-MS. The intracellular Ag content of MCF-7 (15.02 μg Ag/1 × 10^5 cells), MDA-MB-231 (10.46 μg Ag/1 × 10^5 cells), and MCF-10A (3.44 μg Ag/1 × 10^5 cells), consistent with the previous series of results, was confirmed, and the degree of endocytosis and uptake efficiency affected the subsequent toxicity (Fig. S13, ESI†). AgTeNPs were stably present in physiological solutions, but after introduction and accumulation into cells, they were gradually degraded by cytosolic metabolism followed by the release of Ag cations. Releasing Ag cations induces the generation of intracellular reactive oxygen species (ROS) and express substantial toxicity and apoptosis (Fig. S14, ESI†). Given the fact that most cancer cells show very high metabolic activity compared to normal cells, the toxicity caused by metabolic degradation corresponds to the anticancer property of the AgTeNPs.

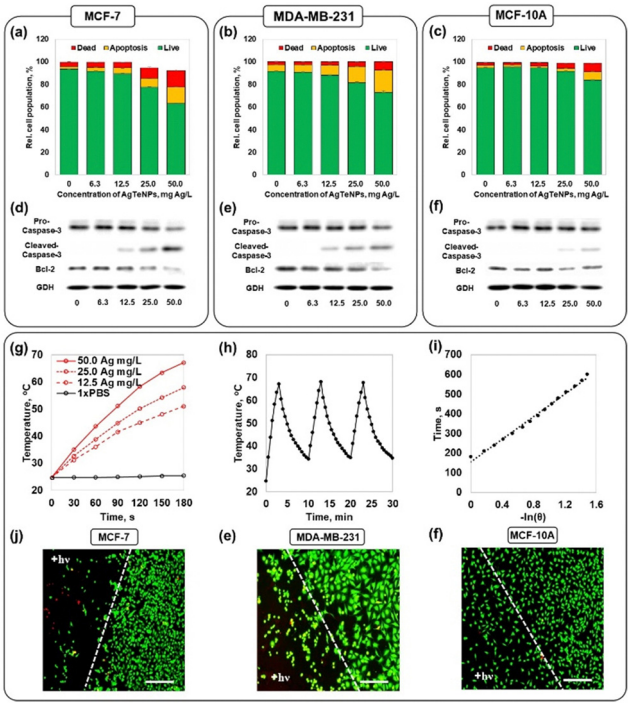

Fig. 5 Verification of nano- and photo-therapeutic efficiency of AgTeNPs against three types of cell lines. (a–c) Apoptosis assay and (d–f) apoptotic protein expression assay for AgTeNP concentrations against MCF-7, MDA-MB-231, and MCF-10A cells. (g) Photothermal conversion mediated temperature elevation, (h) heating–cooling cycle test, and (i) efficiency plotting of AgTeNPs in quartz cuvette cells. (j–f) *In vitro* hyperthermic cell ablation under 808 nm diode laser irradiation. The scale bars are 250 μm.

We also considered an additional photo-therapeutic potential based on the photothermal conversion predicted from the superior NIR absorption of AgTeNPs. 808 nm diode laser irradiation (4 W cm^{-2} for 180 s) was performed on AgTeNPs at various concentrations contained in a quartz cuvette, and the temperature elevation over time was measured using a thermocouple. Unlike the control (1xPBS without AgTeNPs) in which a negligible temperature elevation was observed (ΔT1xPBS = 25.4 °C), the AgTeNPs dispersion showed a clear heat dissipation through the photothermal conversion effect. It was also confirmed that the final temperature and the elevation width measured after laser irradiation were dependent on the particle concentration as $T_{f,\ 50.0\ Ag\ mg\ L^{-1}}$ = 67.2 °C ($\Delta T_{50.0\ Ag\ mg\ L^{-1}}$ = 42.5 °C), $T_{f,\ 25.0\ Ag\ mg\ L^{-1}}$ = 58.0 °C ($\Delta T_{25.0\ Ag\ mg\ L^{-1}}$ = 33.3 °C), and $T_{f,\ 12.5\ Ag\ mg\ L^{-1}}$ = 51.1 °C ($\Delta T_{12.5\ Ag\ mg\ L^{-1}}$ = 26.4 °C) (Fig. 5g).

According to the thermal-cycle test, AgTeNPs exhibited sufficient thermal stability from repeated heating and cooling (Fig. 5h). Photothermal conversion efficiency was calculated to be 61% (Fig. 5i).[46]

Next, to confirm the feasibility of hyperthermic cell ablation in the selective region based on the verified high-efficiency photothermal conversion, AgTeNPs treatment, laser irradiation, and subsequent live/dead staining were performed on each cell line. A relatively sharp boundary was observed for MCF-7 from the fluorescence microscope image of the laser irradiation spot edge (Fig. 5j). In the case of MDA-MB-231, a few live cells

remained in the irradiation region, and normal cell line MCF-10A induced a slight decrease in cell density without severe ablation (Fig. 5k and l). The difference in the ratio of live and dead cells was due to the uptake efficacy of the heat-generating particles within the cell.

From the quantitative *in vitro* test, it was possible to confirm the synergistic effect of nano-therapy induced by the metabolic degradation of introduced AgTeNPs and photothermal therapy (PTT) under NIR laser irradiation. According to the cell viability assay, 50 mg Ag per L of AgTeNPs treatment dramatically reduced the viability in the order of MCF-7 (63.3% viable), MDA-MB-231 (74.9% viable), and MCF-10A (93.2% viable). NIR irradiation without particle incorporation did not induce apoptosis at all, as did the control set (1xPBS). The therapeutic efficacy of PTT was maximized in MCF-7 cells (5.0% viable), followed by MDA-MB-231 cells (26.1% viable), and in MCF-10A cells, a lower percentage of dead cells (68.3% viable) was observed compared to breast cancer cell lines (Fig. 6a). Additionally, for each experimental condition, nuclei, live cells and dead cells were stained with Hoechest 33342, Calcein AM, and ethidium homodimer-1 (EthiD-1), respectively (Fig. 6b). Finally, it was verified that all *in vitro* results, including selective toxicity and combinatorial therapeutic effect, were consistently obtained.

Before entering the full-scale *in vivo* evaluation using the mouse model, verification of *in vivo* toxicity and distribution was done. Assuming that the delivery of nanoparticles *in vivo* is achieved through intravenous (IV) injection, whether or not to induce hemolysis is an important requirement. When AgTeNPs in various doses were added to red blood cells harvested from the male BALB/c-nude mouse, there was no hemolysis even in the maximum dose (100 Ag mg L^{-1}) (Fig. S15, ESI†).

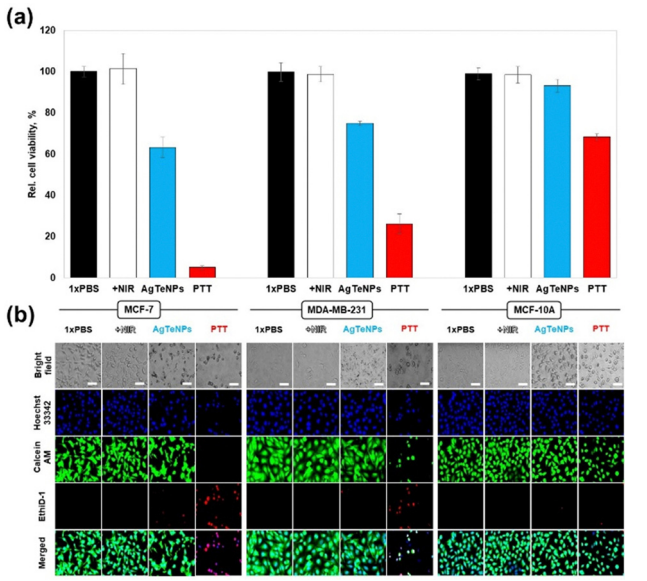

Fig. 6 *In vitro* quantitative therapeutic efficiency verification of AgTeNPs. (a) Cell viability comparison against MCF-7, MDA-MB-231, and MCF-10A cells. (b) Fluorescence microscopy images for each test condition with appropriate staining for nuclei (Hoechst 33342, blue), live cells (Calcein AM, green), and dead cells (EthiD-1, red). The scale bars are 50 μm.

Next, acute toxicity (single injection with high dose) and chronical toxicity (multi-injection with pre-clinical dose) were characterized *in vivo* using male BALB/c-nude mice. According to the histological analysis for acute and chronical toxicity, there was no abnormalities including tissue lysis or disruption against representative major organs (heart, liver, lung, spleen, and kidney) compared to the negative control (1xPBS injected mice) (Fig. S16, ESI†). In the hematological analysis, there was no significant difference in circulating blood cell counts (Fig. S17a–c, ESI†). Moreover, a similar tendency in the serological analysis was observed for the expression level of biomarkers indicating organ toxicity. Hepatoxicity indicator aminotransferase (AST) and alanine aminotransferase (ALT), renal toxicity indicator blood urea nitrogen (BUN) and creatinine (Crea) levels were consistent with those of the control group (Fig. S17d–g, ESI†). Total protein level (TP) and lactate dehydrogenase (LDH) are biomarkers that generally indicate chronic toxicity and cell damage, respectively, and there was no distinctive adverse effect from the injection of AgTeNPs (Fig. S17h and I, ESI†).

To confirm *in vivo* bio-distribution and tumor accumulation efficacy of AgTeNPs, the particles were IV injected into two different xenograft mouse models, MCF-7 and MDA-MB-231. After 24 h of injection, the major organs (heart, liver, lung, spleen, and kidney) and tumor tissue were harvested and subjected to ICP-MS analysis to quantify the introduced Ag amount. In the MCF-7 xenograft model, most of the injected particles accumulated in the liver (17.30 μg Ag), followed by tumor (1.97 μg Ag) and kidney (1.80 μg Ag), and this *in vivo* distribution tendency of the MCF-7 xenograft model was similarly observed in MDA-MB-231 (Fig. S18a, ESI†). The injected particles mainly accumulated in the liver (14.96 μg Ag), kidney (1.64 μg Ag), and tumor (1.37 μg Ag) (Fig. S18b, ESI†). During all kinds of toxicity tests, no abnormal behaviors including breathing, convulsions, defecation, and cyanosis were observed. The series of pre-clinical toxicity studies proved that AgTeNPs have excellent biocompatibility, making them suitable for further therapeutic applications at the animal level.

For demonstrating *in vivo* cancer therapeutic evaluation by AgTeNPs, MCF-7 cells or MDA-MB-231 cells were subcutaneously injected into the right flank for xenograft model formation. When the tumor volume reached ~50 mm^3, 1xPBS or AgTeNPs (5 μg Ag/g mouse body weight) was injected through the mice tail vein. After 24 h of injection, 808 nm laser irradiation was performed in the tumor tissue region. The injection and laser irradiation were repeatedly conducted three times at an interval of 6 days (day 0, 6, and 12). In the case of the active metabolic MCF-7 xenograft model, even group treated only with AgTeNPs exhibited a tumor suppression effect with a 42.7% reduction in tumor size (ΔV_{tumor} = 19.9-fold) due to the accumulation of AgTeNPs, which induced cancer cell apoptosis (Fig. 7a). Further application of PTT following NIR irradiation showed an 83.9% tumor growth inhibitory effect (ΔV_{tumor} = 5.6-fold). Although complete tumor tissue annihilation was not achieved under the tested amount of AgTeNPs and NIR irradiation conditions, there was a definite therapeutic effect compared to the tumor growth identified in 1xPBS (ΔV_{tumor} = 34.7-fold) or NIR only

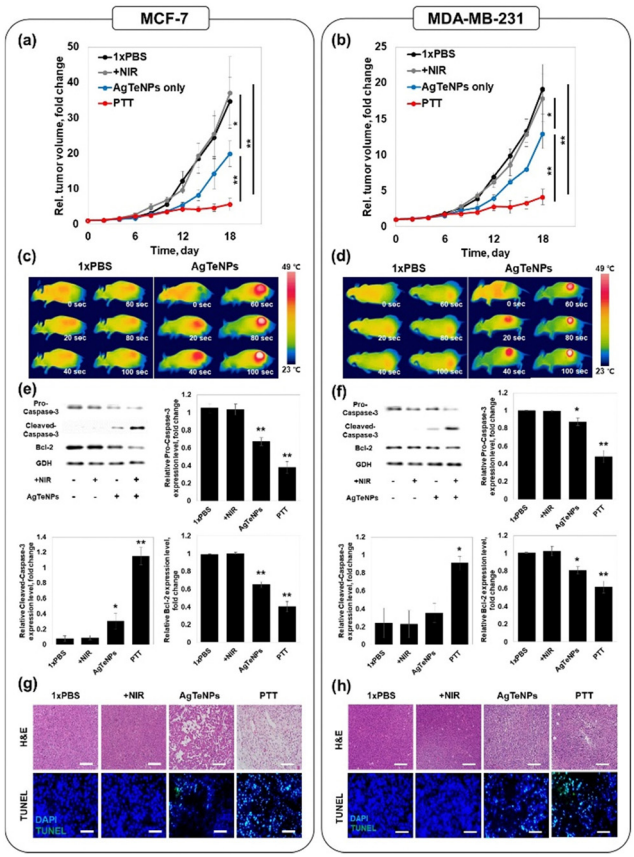

Fig. 7 *In vivo* photo-nano breast cancer therapy by IV injected AgTeNPs. (a and b) Relative tumor volume changes for xenograft mice. (c and d) Thermographic camera image for 808 nm laser irradiation. (e and f) *In vivo* protein expression comparison, (g and h) H&E staining, and TUNEL assay for the photo-nano therapy-treated tumor tissue. The scale bar is 50 μm.

(ΔV_{tumor} = 37.2-fold) used as control conditions. The relative change of tumor size in the MDA-MB-231 xenograft model showed a similar tendency as observed with the MCF-7 xenograft model. AgTeNPs injection suppressed tumor growth by 32.3% (ΔV_{tumor} = 13.0-fold) and PTT further reduced by 78.6% (ΔV_{tumor} = 4.1-fold) compared to control groups (Fig. 7b). During the pre-clinical sensory evaluation, no significant body weight loss or gain was observed in any mice in the experimental group (Fig. S19, ESI†).

To clearly demonstrate the hyperthermic effect on the tumor tissue region, we observed the real-time temperature increase in the local area of the mouse body using a thermal imaging camera (Fig. 7c and d). When the NIR laser hit the tumor region, only the AgTeNPs bearing mice showed dramatic local heating over 46 °C, which induced irreversible heat-shock to the tumor. In contrast, negligible temperature elevation was observed without AgTeNPs. Thermographic images proved that passive targeting and accumulation of AgTeNPs into the tumor endowed heat dissipation by photothermal conversion, and which inflicts sufficient heat. In the analysis of cell apoptosis protein biomarkers, both MCF-7 and MDA-MB-231 tumors exhibited downregulated expression of pro-caspase-3 and Bcl-2, and upregulated expression of cleaved-caspase-3 as observed during *in vitro* investigation (Fig. 7e, f and Fig. S20, S21, ESI†).

Finally, to evaluate the histological status of the tumor treated with the AgTeNPs-based cancer therapy, histological analysis of the tumor was performed including hematoxylin and eosin (H&E) and terminal deoxynucleotidyl transferase dUTP nick end labeling (TUNEL) staining. Both from MCF-7 and MDA-MB-231, tissue lysis, disruption, or cell death was not detected in the control group. In contrast, AgTeNPs treated tumors showed local tissue disruption and an increased presence of dead cells, and PTT treatment significantly increased tissue disintegration and the presence of dead cells (Fig. 7g and h).

Conclusions

In summary, we successfully synthesized biocompatible AgTeNPs by the solvothermal galvanic replacement of TeNRs templates. After the conventional galvanic replacement reaction, it was confirmed that elliptical nanoparticles were formed through Ostwald ripening and structural disintegration under solvothermal conditions. Toxicity, anticancer effect, and PTT potential were verified for three cell lines including normal cells and breast cancer cells, MCF-7, MDA-MB-231, and MCF-10A. AgTeNPs were found to exhibit negligible toxicity both *in vitro* and *in vivo* despite Ag being the main composition due to their robust structure with high crystallinity and an ionic bonded form as silver telluride on the surface. A more pronounced suppression effect was observed in cells with active cellular metabolism, confirming that the endocytosis of AgTeNPs and their subsequent metabolic degradation, leading to the release of ions, were the main contributing factors. Based on the high absorbance seen in the NIR region, it was also confirmed in the cuvette system that the photothermal conversion effect existed at an excellent level of 61% efficiency. Combined with the innate anticancer effect, PTT showed a highly synergistic therapeutic effect on breast cancer cells *in vitro*. A series of observed trends showed the same results in the *in vivo* evaluation of MCF-7 and MDA-MB-231 xenograft mice models.

Author contributions

Conceptualization: H. Jang. Investigation: S. Kang, H. Ahn, and S. Kim. Formal analysis: S. Kang, H. Ahn, and H. Jang. Visualization and Writing: S. Kang, H. Ahn, D. N. Lee and H. Jang. Supervision: D.-H. Min and H. Jang.

Conflicts of interest

There are no conflicts to declare.

Acknowledgements

This research was supported by the National Convergence Research of Scientific Challenges (NRF-2020M3F7A1094299) through the National Research Foundation of Korea (NRF)

funded by the Ministry of Science and ICT. This research was supported by the Basic Science Research Program through the National Research Foundation of Korea (NRF) funded by the Ministry of Education (NRF-2021R1A2B5B03086506, NRF-2021R1A2C1004285, and 2022R1A2C4001692). The present research has been conducted by the Excellent Researcher Support Project of Kwangwoon University in 2022.

Notes and references

1 X. Nie, F. Gao, C. Liu and Y.-Z. You, *J. Mater. Chem. B*, 2021, **9**, 4006.
2 J. Langer, D. J. de Aberasturi, J. Aizpurua, R. A. Alvarez-Puebla, B. Auguié, J. J. Baumberg, G. C. Bazan, S. E. J. Bell, A. Boisen, A. G. Brolo, J. Choo, D. Cialla-May, V. Deckert, L. Fabris, K. Faulds, F. J. G. de Abajo, R. Goodacre, D. Graham, A. J. Haes, C. L. Haynes, C. Huck, T. Itoh, M. Käll, J. Kneipp, N. A. Kotov, H. Kuang, E. C. L. Ru, H. K. Lee, J.-F. Li, X. Y. Ling, S. A. Maier, T. Mayerhöfer, M. Moskovits, K. Murakoshi, J.-M. Nam, S. Nie, Y. Ozaki, I. Pastoriza-Santos, J. Perez-Juste, J. Popp, A. Pucci, S. Reich, B. Ren, G. C. Schatz, T. Shegai, S. Schlücker, L.-L. Tay, K. G. Thomas, Z.-Q. Tian, R. P. Van Duyne, T. Vo-Dinh, Y. Wang, K. A. Willets, C. Xu, H. Xu, Y. Xu, Y. S. Yamamoto, B. Zhao and L. M. Liz-Marzán, *ACS Nano*, 2020, **14**, 28.
3 T. Liu, X. Li, J. Wang, P. Zhang, X. Huang, Z. Zhang, D.-S. Gua and X. Yang, *J. Mater. Chem. B*, 2020, **8**, 5483.
4 C. Levard, E. M. Hotze, B. P. Colman, A. L. Dale, L. Truong, X. Y. Yang, A. J. Bone, G. E. Brown Jr., R. L. Tanguay, R. T. Di Giulio, E. S. Bernhardt, J. N. Meyer, M. R. Wiesner and G. V. Lowry, *Environ. Sci. Technol.*, 2013, **47**, 13440.
5 G. Baraldi, M. Carrada, J. Toudert, F. J. Ferrer, A. Arbouet, V. Paillard and J. Gonzalo, *J. Phys. Chem. C*, 2013, **117**, 9431.
6 A. R. Gliga, S. Skoglund, I. O. Wallinder, B. Fadeel and H. L. Karlsson, *Part. Fibre Toxicol.*, 2014, **11**, 11.
7 Y. Qing, L. Cheng, R. Li, G. Liu, Y. Zhang, X. Tang, J. Wang, H. Liu and Y. Qin, *Int. J. Nanomed.*, 2018, **13**, 3311.
8 L. M. Moreau, C. A. Schurman, S. Kewalramani, M. M. Shahjamali, C. A. Mirkin and M. J. Bedzyk, *J. Am. Chem. Soc.*, 2017, **139**, 12291.
9 S. Kang, W. Shin, K. Kang, M.-H. Choi, Y.-J. Kim, Y.-K. Kim, D.-H. Min and H. Jang, *ACS Appl. Mater. Interfaces*, 2018, **10**, 13819.
10 S. Kang, W. Shin, M.-H. Choi, M. Ahn, Y.-K. Kim, S. Kim, D.-H. Min and H. Jang, *ACS Nano*, 2018, **12**, 6997.
11 G. Yim, S. Kang, Y.-J. Kim, Y.-K. Kim, D.-H. Min and H. Jang, *ACS Nano*, 2019, **13**, 3434.
12 A. Amirjani, P. Shokarani, S. A. Sharif, H. Moheb, H. Ahmadi, Z. S. Ahmadiani and M. S. Paroushi, *J. Mater. Chem. B*, 2023, **11**, 3537.
13 N. Harbeck, F. Penault-Llorca, J. Cortes, M. Gnant, N. Houssami, P. Poortmans, K. Ruddy, J. Tsang and F. Cardoso, *Nat. Rev. Dis. Primers*, 2019, **5**, 66.
14 S. Loibl, P. Poortmans, M. Morrow, C. Denkert and G. Curigliano, *Lancet*, 2021, **397**, 1750.
15 A. G. Waks and E. P. Winer, *JAMA*, 2019, **321**, 288.
16 M. Mutebi, B. O. Anderson, C. Duggan, C. Adebamowo, G. Agarwal, Z. Ali, P. Bird, J.-M. Bourque, R. DeBoer, L. H. Gebrim, R. Masetti, S. Masood, M. Menon, G. Nakigudde, A. Ng'ang'a, N. Niyonzima, A. F. Rositch, K. Unger-Saldana, C. Villarreal-Garza, A. Dvaladze, N. S. El Saghir, J. R. Gralow and A. Eniu, *Cancer*, 2020, **126**, 2365.
17 J. Adams, P. J. Carder, S. Downey, M. A. Forbes, K. MacLennan, V. Allgar, S. Kaufman, S. Hallam, R. Bicknell, J. J. Walker, F. Cairnduff, P. J. Selby, T. J. Perren, M. Lansdown and R. E. Banks, *Cancer Res.*, 2000, **60**, 2898.
18 H. Masuda, D. Zhang, C. Bartholomeusz, H. Doihara, G. N. Hortobagyi and N. T. Ueno, *Breast Cancer Res. Treat.*, 2012, **136**, 331.
19 J. Swanner, C. D. Fahrenholtz, I. Tenvooren, B. W. Bernish, J. J. Sears, A. Hooker, C. M. Furdui, E. Alli, W. Li, G. L. Donati, K. L. Cook, P.-A. Vidi and R. Singh, *FASEB BioAdv.*, 2019, **1**, 639.
20 A. Bandyopadhyay, B. Roy, P. Shaw, P. Mondal, M. Kr. Mondal, P. Chowdhury, S. Bhattacharya and A. Chattopadhyay, *Nucleus*, 2020, **63**, 191.
21 J. N. Smith, D. G. Thomas, H. Jolley, V. K. Kodali, M. H. Littke, P. Munusamy, D. R. Baer, M. J. Gaffrey, B. D. Thrall and J. G. Teeguarden, *Part. Fibre Toxicol.*, 2018, **15**, 47.
22 L. E. Valenti and C. E. Giacomelli, *J. Nanopart. Res.*, 2017, **19**, 156.
23 A. K. Samal and T. Pradeep, *J. Phys. Chem. C*, 2009, **113**, 13539.
24 Z.-H. Lin, Z. Yang and H.-T. Chang, *Cryst. Growth Des.*, 2008, **8**, 351.
25 T. S. Sreeprasad, A. K. Samal and T. Pradeep, *J. Phys. Chem. C*, 2009, **113**, 1727.
26 U. K. Gautam and C. N. R. Rao, *J. Mater. Chem.*, 2004, **14**, 2530.
27 M. Yang, R. Gui, H. Jin, Z. Wang, F. Zhang, J. Xia, S. Bi and Y. Xia, *Colloids Surf. B*, 2015, **126**, 115.
28 Q. Xiao, Y. Liang, Y. Liu, S. Lu and S. Huang, *Luminescence*, 2017, **33**, 181.
29 G. Wang, J. Liu, L. Zhu, X. Ma, X. Wang, X. Yang, Y. Guo, L. Yang and J. Lu, *Small*, 2019, **15**, 1902945.
30 L. Dong, W. Li, L. Yu, L. Sun, Y. Chen and G. Hong, *ACS Appl. Mater. Interfaces*, 2020, **12**, 42558.
31 P. Jiang, J.-J. Zhou, R. Li, Z.-L. Wang and S.-S. Xie, *Nanotechnology*, 2006, **17**, 3533.
32 C.-M. Park, W. Choi, Y. Hwa, J.-H. Kim, G. Jeong and H.-J. Sohn, *J. Mater. Chem.*, 2010, **20**, 4854.
33 L. Xu, H.-W. Liang, H.-H. Li, K. Wang, Y. Yang, L.-T. Song, X. Wang and S.-H. Yu, *Nano Res.*, 2015, **8**, 1081.
34 V. K. LaMer and R. H. Dinegar, *J. Am. Chem. Soc.*, 1950, **72**(11), 4847.
35 M.-K. Pong, H. I. Elim, J.-X. Chong, W. Ji, B. de, L. Trout and J.-Y. Lee, *J. Phys. Chem. C*, 2007, **111**, 6281.
36 W. Gierlotka, *J. Alloys Compd.*, 2009, **485**, 231.
37 K. Momma and F. Izumi, *J. Appl. Crystallogr.*, 2011, **44**, 1272–1276.
38 R. Takahata, S. Yamazoe, C. Warakulwit, J. Limtrakul and T. Tsukuda, *J. Phys. Chem. C*, 2016, **120**, 17006.

39 P. Li, Y. Han, X. Zhou, Z. Fan, S. Xu, K. Cao, F. Meng, L. Gao, J. Song, H. Zhang and Y. Lu, *Matter*, 2020, **2**, 658.
40 K. J. Chavez, S. V. Garimella and S. Lipkowitz, *Breast Dis.*, 2010, **32**, 35.
41 Y. Qu, B. Han, Y. Yu, W. Yao, S. Bose, B. Y. Karlan, A. E. Giuliano and X. Cui, *PLoS One*, 2015, **10**, e0131285.
42 T. A. Theodossiou, M. Ali, M. Grigalavicius, B. Grallert, P. Dillard, K. O. Schink, C. E. Olsen, S. Wälchli, E. M. Inderberg, A. Kubin, Q. Peng and K. Berg, *NPG Breast Cancer*, 2019, **5**, 13.
43 P. Danhier, P. Bański, V. L. Payen, D. Grasso, L. Ippolito, P. Sonveaux and P. E. Porporato, *Biochim. Biophys. Acta, Bioenerg.*, 2017, **1858**, 556.
44 A. G. Porter and R. U. Jänicke, *Cell Death Differ.*, 1999, **6**, 99.
45 P. E. Czabotar, G. Lessene, A. Strasser and J. M. Adams, *Nat. Rev. Mol.*, 2014, **15**, 49.
46 H. Chen, L. Shao, T. Ming, Z. Sun, C. Zhao, B. Yang and J. Wang, *Small*, 2010, **6**, 2272.

